Biosensors and Bioelectronics 145 (2019) 111730

Contents lists available at ScienceDirect

Biosensors and Bioelectronics

journal homepage: http://www.elsevier.com/locate/bios

Single-cell impedance analysis of osteogenic differentiation by droplet-based microfluidics

Weihua Fan [a,f], Xi Chen [b,c], Yuqing Ge [a,*], Yan Jin [d], Qinghui Jin [e,**], Jianlong Zhao [a,***]

[a] State Key Laboratory of Transducer Technology, Shanghai Institute of Microsystem and Information Technology, Chinese Academy of Sciences, Shanghai, 200050, China
[b] Department of Pathology, The Third Affiliated Hospital of Soochow University, The First People's Hospital of Changzhou, Changzhou, 213003, China
[c] Orthopaedic Institute, Medical College, Soochow University, Suzhou, 215007, China
[d] College of Sciences, Shanghai Institute of Technology, Shanghai, 201418, China
[e] Faculty of Electrical Engineering and Computer Science, Ningbo University, Ningbo, 315211, China
[f] University of Chinese Academy of Sciences, Beijing, 100049, China

ARTICLE INFO

Keywords:
Single-cell impedance analysis
Droplet microfluidics
Microelectrode array
Bone marrow mesenchymal stem cells
Osteogenic differentiation

ABSTRACT

Single-cell analysis is critical to understanding its heterogeneity and biological processes, such as stem cell differentiation, and elucidating the underlying mechanisms of cellular metabolism. New tools to promote intercellular variability studies help elucidate cellular regulation mechanisms. Here an impedance measurement and analysis system was built to monitor the osteogenic differentiation of single bone marrow mesenchymal stem cells (BM-MSCs) in droplets. The biochip including a microelectrode array was designed based on droplet microfluidics and fabricated. A novel theoretical electrical model was proposed to simulate the electrical properties of cells in the droplets. Impedance measurements showed that single cells are substantially heterogeneous during osteoblast differentiation at different stages (days 0, 7, 14 and 21) and different cell passages (passages 6, 7 and 11). This result was consistent with the appearance of two biomarkers (alkaline phosphatase and calcium nodules), which are the gold standard biomarkers of osteoblastogenesis and differentiation. The device enabled highly efficient single-cell trapping, accurate positioning, and sensitive, label-free and noninvasive impedance measurements of individual cells with multiple channels. This system provides a strategy for exploring the processes of osteoblastogenesis and differentiation at the single-cell level and has substantial potential for applications in the biomedical field.

1. Introduction

Single-cell analysis has become an emerging field in biological and biomedical research for insights into heterogeneity between large populations of cells at a high resolution. Improved methods of single-cell technology have provided a better understanding of cell behavior, heterogeneity and lineage fate and of niche cells and signals that regulate their function (Li et al., 2018; Pinho and Frenette, 2019). Various powerful techniques, including flow cytometry (Safford and Bischel, 2019), atomic force microscopy (Kim et al., 2019; Kuznetsova et al., 2007), optical and magnetic tweezers (Gosse and Croquette, 2002; Navas-Moreno and Chan, 2018), and single-molecule fluorescence spectroscopy (Gosse and Croquette, 2002; Zrimsek et al., 2017), have been developed for single-cell analysis. Flow cytometry is a widely used high-throughput technique for single-cell analysis but lacks the ability to analyze intercellular interactions and local environmental control, and other methods require sophisticated equipment and processes that limit their applications (Saeys et al., 2016). There remain substantial challenges associated with single-cell analysis techniques, and there is a need for new methods that are more sensitive, have high temporal and spatial resolutions, and maintain cell viability.

Rapid downscaling of complementary metal oxide semiconductor (CMOS) technology has allowed the possibility of integrating systems onto a single chip, allowing single-cell trapping and ultrafast signal processing at a low power and cost. The integration (Luo et al., 2019a, b) of microfluidic chips and impedance measurements (Chen et al., 2015;

* Corresponding author.
** Corresponding author.
*** Corresponding author.
E-mail addresses: yqge@mail.sim.ac.cn (Y. Ge), jinqinghui@nbu.edu.cn (Q. Jin), jlzhao@mail.sim.ac.cn (J. Zhao).

https://doi.org/10.1016/j.bios.2019.111730
Received 25 June 2019; Received in revised form 21 September 2019; Accepted 21 September 2019
Available online 25 September 2019

Petchakup et al., 2017) into one chip could offer a label-free, noninvasive and quantitative method to assess cellular characteristics. Seshia et al. developed a single-cell detection system based on microfluidic impedance technology to investigate the differentiation of mouse embryonic stem cells at different stages and analyzed changes in the electrical parameters of cells throughout the process of differentiation (Zhou et al., 2016). Kurz et al. developed a microfluidic chip to capture single cells and measure the impedance to monitor subtonic effects on cell membranes (Kurz et al., 2011). In particular, capacitively coupled contactless conductivity detection (C4D) could provide a noninvasive, highly sensitive and stable approach. C4D microchip sensors have been reported to detect cells (Panke et al., 2011; Tuma, 2017; Weyer et al., 2016). A very thin insulating layer (SiO_2) not only remains transparent for imaging but also isolates electrodes from the solution, reducing electrode polarization (EP) (Ishai et al., 2012, 2013). However, in these studies, single cells in the environment were interlinked with fluid in the lumen, which may hinder data acquisition from single cells.

Droplet microfluidics (Casadevall i Solvas and deMello, 2011) has become an attractive technology for single-cell analysis due to its suitable compartments that are on the same size scale as cells. The advantages of droplet microfluidics include manipulability, reduced sample volumes, high-throughput analysis and a stable local environment. Droplet microfluidics involves various designs that have been developed to achieve single-cell trapping using hydrodynamic forces (Tanyeri et al., 2010). And single cells capsulated by droplets were high-efficiency trapped based on fluid microfluidics in our previous work (Fan et al., 2019). A thin oil layer between an aqueous droplet and a channel wall is the main limitation for the use of impedimetric methods in the detection of cells in droplets. Recently, agglutinated red blood cells and mouse myeloma cells were detected inside microdroplets using advanced detection systems and conductivity-adjusted solutions (Kemna et al., 2013; Marcali and Elbuken, 2016). While the microsystem integrated droplet microfluidics with impedance measurements into a single chip, single-cell analysis was difficult.

In this study, as the extension of our early research, an impedance analysis system integrated with droplet microfluidics and a microelectrode array was designed and fabricated to monitor the osteogenic differentiation of single bone marrow mesenchymal stem cells (BM-MSCs) in droplets (Fig. 1). Single cells were encapsulated by droplets, which were generated by a T-junction (Fig. 1a). Then, the droplets encapsulating single cells were trapped by a main bypass structure and positioned above the electrodes (Fig. 1b). When the frequency-dependent excitation signals were implemented in cell droplets, osteoblastic differentiation of single BM-MSCs was monitored by the impedance spectrum (Fig. 1c). A novel theoretical electrical model of cell droplets based on a single-shell model was proposed to explain the inner phenomenon of single cells in the droplets under a frequency-dependent excitation signal. The ability of the droplets to compartmentalize individual cells provided a stable microenvironment that did not affect cell morphology during device capture and detection. The microsystem integrated with droplet microfluidics and a microelectrode array offers sensitive, label-free and noninvasive methods for single-cell detection. Furthermore, it provides a strategy for exploring cellular behavior, heterogeneity and lineage fate at the single-cell level.

2. Material and methods

2.1. Chip design and fabrication

The biochip consisted of a substrate layer, an electrode layer, an insulating layer and a construction layer, as shown in Fig. 2a. The substrate layer consisted of a piece of glass, the electrode layer consisted of Au/Ti, the insulating layer consisted of SiO_2 deposited by plasma enhanced chemical vapor deposition (PE-CVD), and the construction layer consisted of polydimethylsiloxane (PDMS) with the designed structure. The Au/Ti electrodes were fabricated by the lift-off process. First, the substrates were patterned using an LC100A photoresist. Then, the substrate was coated with Ti as an adhesion layer followed by a specific metal (Au for the electrodes). Next, the gold that was covered by the photoresist was removed by immersing the chip in acetone, and the gold that was not covered by the photoresist remained on the substrate. Then, the insulating layer was formed by depositing SiO_2 on the electrode layer through a PE-CVD process. Finally, the SiO_2 that covered the electrode pads was removed by the deep reactive ion etching (DRIE) process.

For the construction layer, the fabrication techniques were the same as those employed in our previous study (Fan et al., 2019). First, SU-8 3050 was spun onto a 4-inch wafer at approximately 2500 rpm for 45s and baked at 95 °C for approximately 45min. Second, it was exposed under near-ultraviolet light for approximately 205s and baked for 3min from 25 to 95 °C. After the wafer naturally cooled to room temperature, it was developed and rinsed. Then, PDMS was poured onto the wafer, heated at 65 °C for approximately 30min, pealed from the wafer and protected by electrostatic removal of the dust film. The final chip was fabricated by aligning and bonding the construction layer with the electrode chip (Fig. 2d). The whole device is shown in Fig. 1d.

2.2. Cell preparation

Human BM-MSCs (Cyagen Biosciences Inc., Guangzhou, China) were cultured in alpha minimum essential medium (α-MEM; Thermo Fisher Scientific, Waltham, MA, USA) supplemented with 10% fetal bovine serum (FBS; Thermo Fisher Scientific), 100U/mL penicillin, and 100 μg/mL streptomycin (Thermo Fisher Scientific) in a humidified 37 °C/5% CO_2 incubator. The medium was changed every three days. BM-MSCs were passaged for two passages to obtain enough cells for the subsequent experiments. To induce the differentiation of BM-MSCs into the osteogenic lineage, the cells were incubated in osteogenic differentiation medium (OM) consisting of Dulbecco's modified Eagle medium (DMEM; Thermo Fisher Scientific), 10% FBS, 100U/mL penicillin, 100 μg/mL

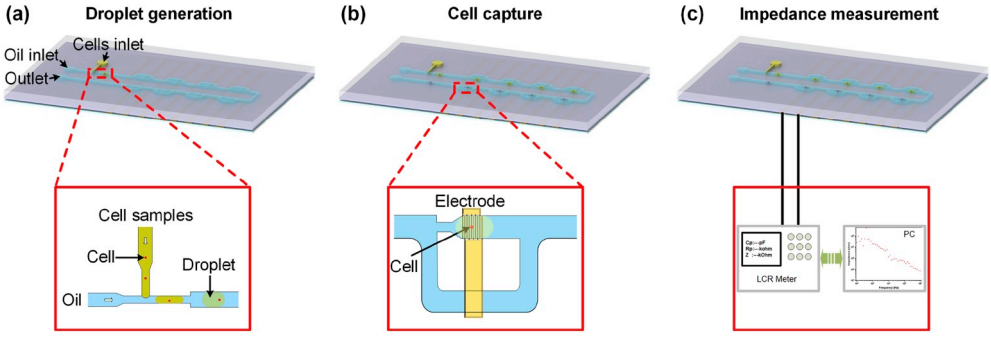

Fig. 1. A diagram of the system based on biochip-integrated Au electrodes. (a) A microdroplet encapsulating a single cell generated by the T-junction. (b) A cell trapped by the main bypass structure above the electrodes. (c) The impedance measured by an impedance analyzer and computer.

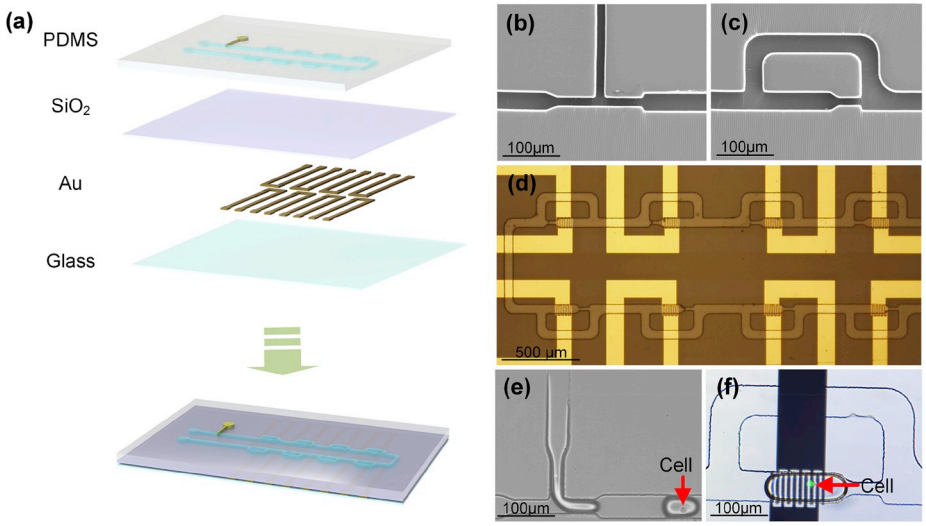

Fig. 2. Images of the structure of the chip. (a) The biochip consisted of a glass substrate, patterned electrodes, SiO_2 insulating layer and PDMS layer. Scanning electron microscopy images of (b) the T-junction that generates the droplets and (c) the main bypass that traps single cells. (d) A top-view image of the chip with PDMS aligned and bonded with the electrode layer. (e) An image of a droplet generated by the T-junction. (f) An image of a single cell trapped above the electrodes by light and fluorescence microscopy.

streptomycin, 50 μg/mL L-ascorbic acid, 100 nM dexamethasone, and 10 mM β-glycerol phosphate (Sigma-Aldrich) for 21 days. The size of BM-MSCs was about 10 μm.

2.3. Alkaline phosphatase (ALP) and Alizarin Red S staining

Intracellular ALP activity was analyzed using commercially available kits after 0, 7, 14 and 21 days of osteogenic induction. To qualitatively observe ALP-positive cells, BM-MSCs were washed three times with PBS, fixed with 4% paraformaldehyde, and stained with a BCIP/NBT Alkaline Phosphatase Color Development Kit for 15 min according to the manufacturer's instructions. Digital images were acquired using an upright microscope. Mineralization of the matrix was determined by Alizarin Red S staining. At day 21, differentiated BM-MSCs were fixed in 4% paraformaldehyde and incubated in 1% Alizarin Red S solution (pH = 4.3; Sigma-Aldrich) at room temperature for 15 min. After washing the cells twice with PBS, images of matrix mineralization were acquired using a microscope (IX73, Nikon Corporation).

2.4. Total RNA extraction and real-time reverse transcription polymerase chain reaction (RT-PCR)

Total RNA was extracted using TRIzol reagent (TaKaRa Bio, Otsu, Shiga, Japan), and 1 μg of total RNA was reverse-transcribed using a PrimeScript™ RT Master Mix Kit (TaKaRa Bio). To quantify mRNA expression, an amount of cDNA equivalent to 20 ng of total RNA was amplified by real-time PCR using an iTap Universal SYBR Green Supermix Kit (Bio-Rad, Hercules, CA, USA). Transcript levels of the osteogenic marker gene ALP and the internal standard gene GAPDH were evaluated. The primers were as follows: ALP (forward, 5′-AGCACTCCCACTTCATCTGGAA-3'; reverse, 5′-GAGACCCAA-TAGGTAGTCCACATTG-3'; GenBank accession: NM 000478.3) and GAPDH (forward, 5′-AGAAAAACCTGCCAAATATGATGAC-3'; reverse, 5′- TGGGTGTCGCTGTTGAAGTC-3'; GenBank accession: NM 002046). Real-time PCR was performed on a CFX96TM Real-Time PCR System (Bio-Rad) following the manufacturer's protocol. Relative transcript levels were calculated as follows: $\chi = 2-\Delta\Delta Ct$, where $\Delta\Delta Ct = \Delta E - \Delta C$, $\Delta E = Ctexp - CtGAPDH$, and $\Delta C = Ctct1 - CtGAPDH$.

2.5. Impedance measurements

The microfluidic chip was glued on a custom-made printed circuit board (PCB). The electrodes were connected to the PCB through a copper wire, and the PCB was connected to the impedance analyzer, which controlled the digital signal to switch between analysis units and provided the interface to a computer for impedance measurements. Prior to cell characterization, the device was first filled with mineral oil, and a calibration measurement was performed to calibrate the device. This calibration measurement served as a baseline for further cell impedance measurements. Then, BM-MSCs were injected into the device to form microdroplets in which the cell was suspended and about a sphere. After all traps were occupied by microdroplets (observed by microscopy), cell injection was stopped. Cell impedance was measured by an impedance analyzer, and a 100 mV input was used. The frequency range was from 100 Hz to 1 MHz, and 10 points were measured per decade. During the impedance measurements, fluid flow was stopped to minimize deformation of the droplets caused by fluid shear stress. Bright-field images, which were used to verify cell differentiation stages, of cells dyed by the BCIP/NBT alkaline phosphatase color development kit (Beyotime Biotechnology, China) were observed by a microscope. As shown in Fig. 1, the distance between two microdroplets was very short, providing nearly the same environment for two microdroplets, reducing or even eliminating the effects of different environmental factors. The dispersed phase consisted of 3% ABIL EM90 and 0.1% TritonX-100 in mineral oil (X. Bian et al., 2015). Images were obtained using fluorescence microscopy (IX73, Nikon, Japan). Impedance spectroscopy was conducted by Interface 1000 instrumentation (Garmy Instrument).

3. Results and discussion

3.1. Chip structure and fabrication

The components of the chip are shown in Fig. 2. The components enabled droplet generation (Fig. 2b and e), cell encapsulation, cell capture (Fig. 2c and f) and impedance measurement functionalities. The chip included a substrate, electrodes, insulating layer and construction layer (Fig. 2a). The processes are described in the experimental section in detail. Briefly, the electrode layer was fabricated by a standard lift-off process. The insulating layer was fabricated by PE-CVD, and the PDMS layer was fabricated by conventional soft lithography and photolithography techniques (He et al., 2005; X. Bian et al., 2015). The substrate consisted of glass that had a thickness of 400–500 μm, and the thicknesses of Au/Ti were 1000/300 Å. The insulating layer had a thickness of 100 nm, and the thickness of PDMS was 50 μm. The electrodes were designed as interdigital electrodes (IDEs), which offer a high sensitivity, good stability and great signal-to-noise ratio (Roy and Gao, 2009), and fabricated as shown in Fig. 2f. The number of fingers was 5, the widths of the fingers and gaps were 9 μm, and the length of the fingers was 60 μm.

The generation of droplets by the T-junction (Fig. 2b) was simple and controllable (Chakraborty et al., 2019). The capture structure (the main bypass structure) (Fig. 2c) was designed and fabricated by fluid mechanics (Tan and Takeuchi, 2007). An overview of the chip is shown in Fig. 2d.

3.2. Cell encapsulation and capture

Single-cell analysis was based on the Poisson distribution (Shapiro, 2003) of cells in the microdroplets. As shown in equation (1), P (X = k) is the probability of k cells per microdroplet, where λ is the mean number of cells per microdroplet.

$$P(X=k)=\frac{e^{-\lambda}}{k!}\lambda^{k} \tag{1}$$

The construction was described in a previous study, and the droplets were formed at the T-junction and trapped by the main bypass construct. The cell concentration was 1.67×10^{6} cells/mL, and the single-cell capture efficiency reached up to 60% in our earlier research (Fan et al., 2019), once a microdroplet encapsulating two or more cells was trapped in the main channel in Fig. 2c, the microdroplet was released by oil until microdroplet encapsulating one single cell.

3.3. Theory and model

As the cell structure and composition change with cell progression, the membrane capacitance and cytoplasmic conductance adjust to reflect these phenotypic changes (Sano et al., 2011; Vahey and Voldman, 2009). Information about physiological cell properties can be extracted by the membrane capacitance and cytoplasmic conductance from a suitable model. For the model of microdroplets encapsulating one cell, the presence of the microdroplets should be considered in conventional impedance theory, and the single-shell model (Gimsa, 2001; Prodan et al., 2008) by the Pauly-Schwan theory is not justified. To overcome this problem, a cell droplet model was proposed (Fig. 3b), and the blank model is shown in Fig. 3a. When a cell is encapsulated by a microdroplet, the electric model of the interface of the microdroplet can be considered a membrane, and its function is physically isolated and is considered a small negligible capacitor. For biological cells with a lipid bilayer plasma membrane, the lipid bilayer plasma membrane is considered a capacitor, and the cytoplasm is regarded as resistance. Then, the effective circuit can be simplified, as shown in Fig. 3c and d, and the capacity of the cell membrane can be calculated by equation (2) as follows:

$$C_m \approx \frac{Z_{Im}^{'}-Z_{Im}}{2\pi f {Z_{Re}}^{2}} \tag{2}$$

where $Z_{Im}^{'}$ and Z_{Im} are imaginaries of different measurements of the blank structure and a droplet within the capture structure, respectively. The detailed process is described in the supporting information.

To detect intracellular changes, an electric field penetrates the cell membrane. Information on the molecular orientation and counterion redistribution is obtained from the dielectric spectra of cell suspensions. It depends on the magnitude $\Delta\varepsilon$ and the characteristic frequency f_c, which are essentially predicted from the single-shell model, of a dielectric dispersion due to interfacial polarization. The dielectric behavior of cell suspensions was analyzed using Maxwell's mixture theory. The electric field distribution was simulated by COMSOL from 100 Hz to 1 GHz, the suitable result was shown in Fig. 4. At a low frequency (1995.5 Hz), the electrical field did not penetrate the cell, indicating that it is not possible to analyze intracellular changes by the electric field. At a high frequency (1 GHz), the cell did not affect the electric field. At a frequency of 100 kHz, the electric field penetrated the cell, which was suitable for the detection of intracellular changes.

The detailed values of the factors are shown in Table 1. The characterization frequency (f_c) provided the best response to the cell. The characteristic frequency was calculated by the following equation (Asami, 2002; Pauly and Schwan, 1959):

$$\tau=\frac{1}{2\pi f_c}=RC_m\left(\frac{1}{\sigma_i}+\frac{1-\phi}{2+\phi}\frac{1}{\sigma_a}\right) \tag{3}$$

where σ_i and σ_a are the conductivity of the cytoplasm and the external medium, respectively, Φ is the cell fraction, and R is the cell radius. Furthermore, C_m is the capacitance of the cell, which is defined as follows (Asami, 2002):

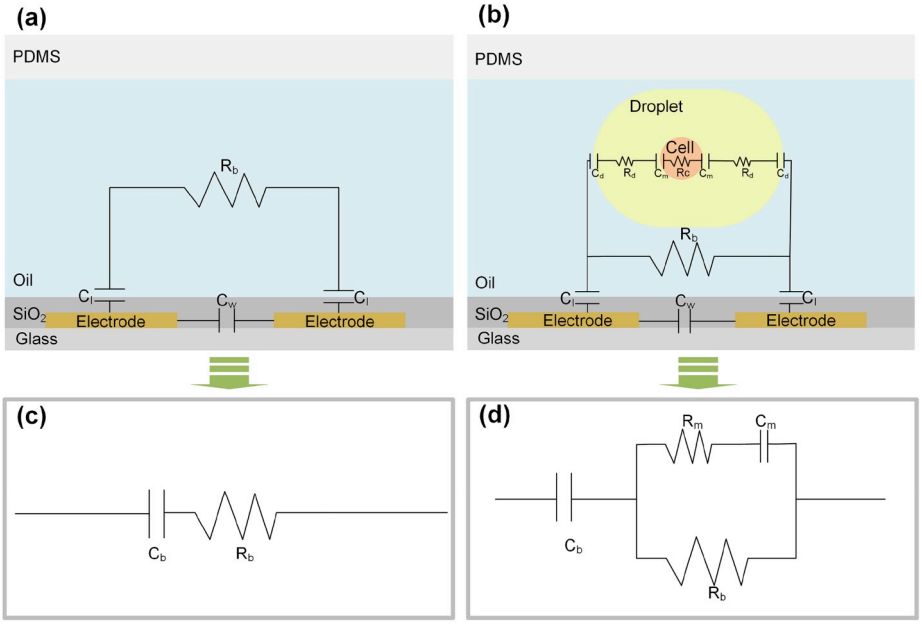

Fig. 3. (a) The circuit model of the blank device in mineral oil. (b) The circuit model of the cell droplet; (c), (d) The corresponding circuit models of (a) and (b). R_b, R_c and R_d are the resistances of the bulk, cytoplasm and droplet, respectively, C_w, C_I, C_d and C_m are the capacitances within the electrodes, insulating layer, droplet and cell membrane, respectively. The simplified circuit of the blank device and cell droplet, and the C_w and C_d can be neglected compared with C_m and C_I, respectively.

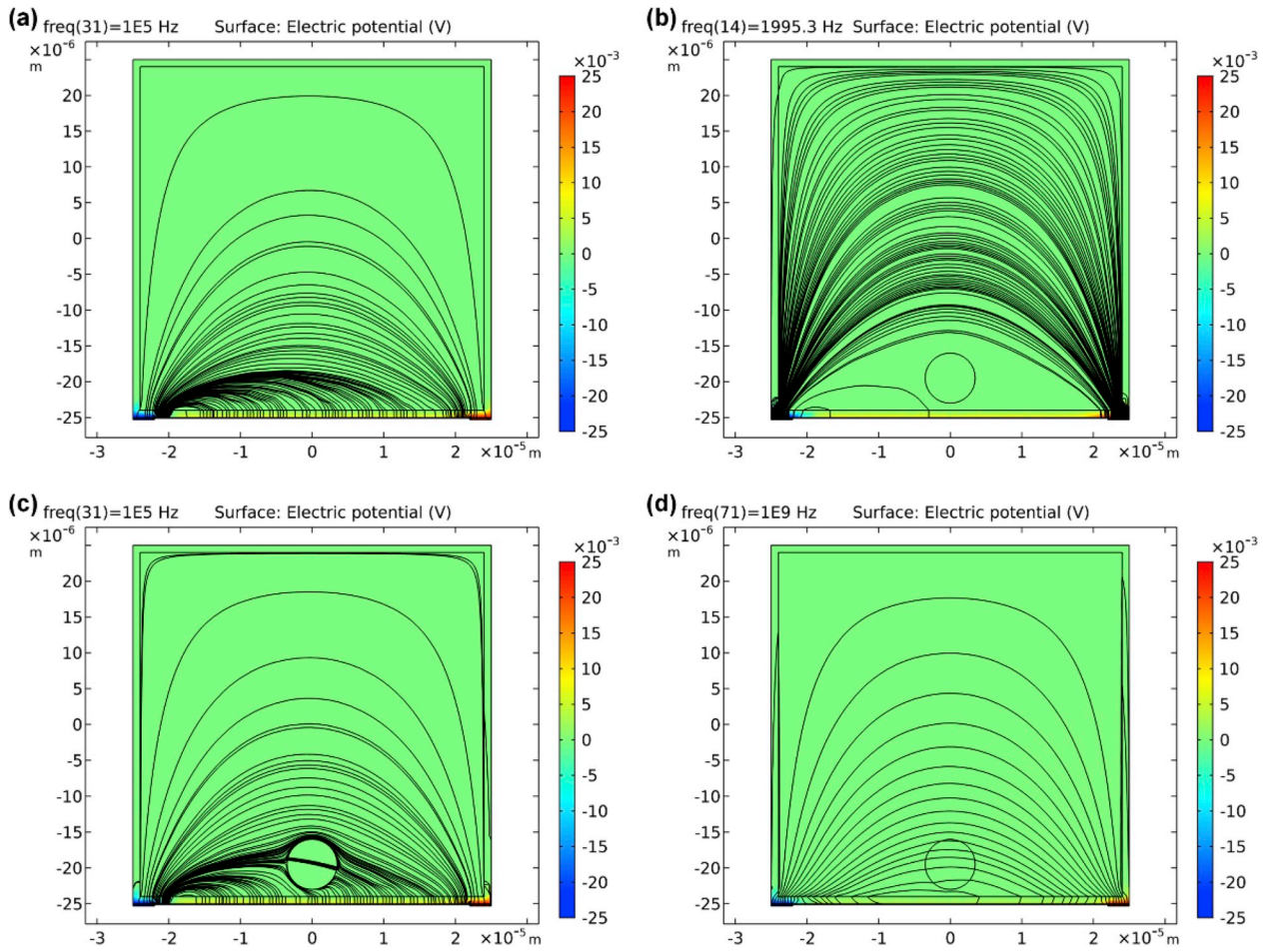

Fig. 4. The results of the simulation by COMSOL. The distributions of the electric potential and electric field of (a) a blank droplet (100 kHz) and droplets encapsulating a single cell at (b) 1995.3 Hz, (b) 100 kHz, (d) and 1 GHz.

Table 1
The values of the dimensions, permittivities and conductivities.

R [m]	V_c [m^3]	L [m]	W [m]	H [m]	V_d [m^3]
4.00E-06	2.68E-16	1.00E-04	5.00E-05	5.00E-05	2.50E-13
ε_0 [F/m]	ε_m	σ_i [S/m]	σ_a [S/m]	φ	D [m]
8.85419E-12	20	0.018	41.3	1.07E-03	1.00E-08

Where ε_0 and ε_m are the permittivity of vacuum and relative permittivity, respectively. φ Is the volume fraction. σ_i and σ_a are the conductivities of the cytoplasm and external medium, respectively.

$$C_m = \frac{\varepsilon_m \varepsilon_0}{d} \quad (4)$$

where ε_m and ε_0 are the dielectric constants of air and cell membranes, respectively, and d is the thickness of the cell membrane. The external medium was OM, which had a conductivity of 41.3 S/m, a σ_i of 0.018 S/m, and an f_c of approximately 100 kHz for an R of 4 μm (Table 1). The value was different from that of the dielectric dispersion of protein solutions (1–10 MHz) (Asami, 2002). In fact, the electric field and current density were not uniform. At frequencies that were lower (Fig. 4a) than the f_c, information on the cytoplasm was difficult to obtain because the electric field strength in the cytoplasm was very small owing to the insulating plasma membrane. Information on the cytoplasm was obtainable at frequencies that were higher (Fig. 4d) than the f_c, where the insulating membrane was short circuited. At the f_c (Fig. 4c), the electric field penetrated the cell membrane to detect information regarding intercellular substances.

3.4. Impedance throughout cell differentiation

Impedance spectroscopy of single cells was conducted at days 0 (predifferentiation), 7, 14 and 21, as shown in Fig. 5. Differentiated cells at day 21 typically provided more pronounced responses compared with responses provided by undifferentiated cells (at day 0). The impedance variation between individual cells, which was an indication of cell heterogeneity, was found to be the largest for certain cells that were differentiated at day 0. Fully differentiated (at day 21) cells exhibited less heterogeneity than cells in the transition state (at days 7 and 14). The impedance of cells at days 0 and 7 showed similar heterogeneity but greater heterogeneity than cells at days 14 and 21. A greater variation in the impedance was observed as the differentiation time decreased at 100 kHz (Fig. 6a). Decreasing impedance was obviously observed from days 7–21, but the impedances at days 0 and 7 were similar, suggesting that in the first week of differentiation, the transport of ions, such as Ca^{2+}, was not sufficient from the intracellular space to the droplet, and after a week, calcium ions gradually formed (Hankemeier et al., 2005; Luo et al., 2019a, b). Throughout the process of differentiation, the morphology (Fig. 5a1, b1, c1, and d1) of the cells changed significantly from a star-like shape to a fibroblast-like shape. Alkaline phosphatase (ALP), which is an early-stage osteogenic marker, was analyzed by real-time polymerase chain reaction (RT-PCR) for absolute quantification and by staining for relative quantification. The relative quantity of ALP (Fig. 5a2, b2, c2, and d2) reached maximum levels in the first week of culture in OM and then decreased, remaining relatively stable, which was consistent with a previous report (Frank et al., 2002). Similarly, RT-PCR analysis confirmed that the expression

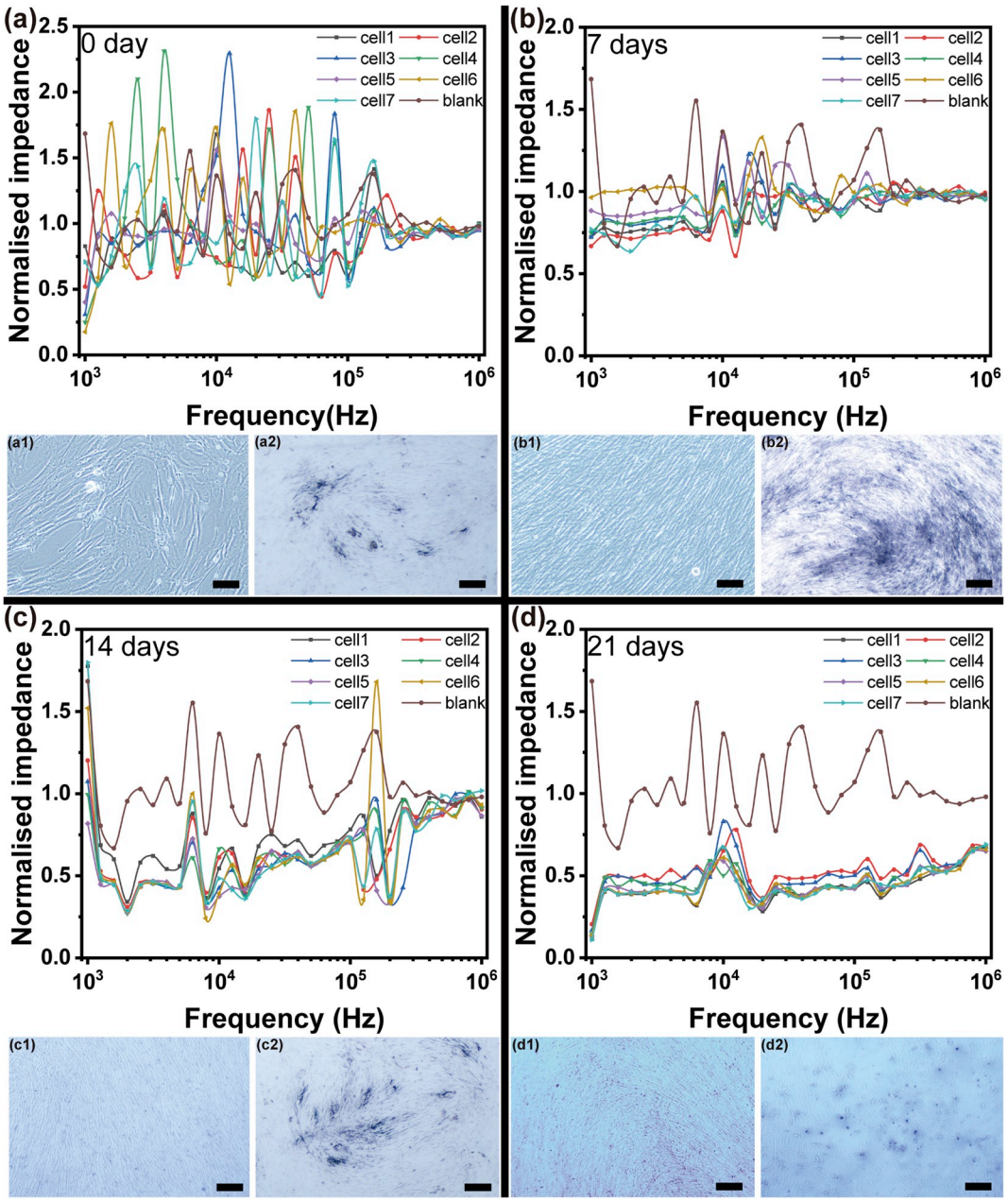

Fig. 5. The impedance spectra of different cells at different stages of BM-MSC differentiation: (a) day 0, (b) day 7, (c) day 14, (d) and day 21. Light microscopy images of cells on different days (a1, b1, c1, d1); Images (a2, b2, c2, d2) of alkaline phosphatase-stained cells at different stages. The blue area indicates alkaline phosphatase staining by the BCIP/NBT Alkaline Phosphatase Color Development Kit. The scale bars indicate 500 μm. The number of cells analyzed at each stage was seven. (For interpretation of the references to color in this figure legend, the reader is referred to the Web version of this article.)

of ALP was significantly upregulated in differentiated BM-MSCs. Compared with ALP expression in undifferentiated cells, ALP expression was 8.3-fold greater on day 7 and 2.0-fold greater on day 14 (Fig. 6b).

3.5. Impedance of different cell passages

Impedance spectroscopy throughout osteogenic differentiation of different cell passages was analyzed, as shown in Fig. 7a. An obvious decrease in the impedance was observed from days 7–21, which was consistent with an increase in charged substances, such as DNA, over time as described in previous reports (Frank et al., 2002; Jansen et al., 2010). The impedance of cells in the sixth and seventh passages increased from days 0–7 and decreased from days 7–21 and had a similar trend, while changes in the impedance of cells in the eleventh passage were contrary to those of cells in the sixth and seventh passages at 100 kHz, indicating that cells in the sixth and seventh passages had good differentiation performance. Calcium deposition indicated a mature osteoblastic phenotype, as shown in Fig. 7b, c and 7d, which is in agreement with the impedance data. In addition, it has been reported that cells at certain passages may undergo a process of replicative senescence in vitro, where MSCs gradually lose their proliferative ability and multilineage differentiation potential. Mineralization of the extracellular matrix (ECM), as indicated by staining with Alizarin Red S dye, demonstrated that replicative senescence by in vitro passaging impaired the differentiation of BM-MSCs into the osteoblast lineage. BM-MSCs in the sixth passage on day 21 showed denser staining than those in the other two groups. Mineralized areas in cells in the seventh and eleventh

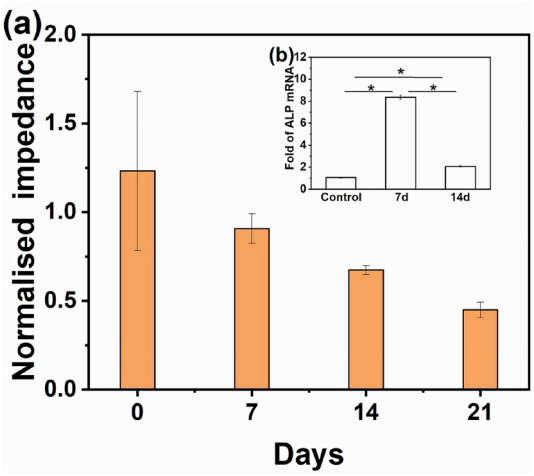

Fig. 6. (a) The impedance spectra of BM-MSC differentiation at days 0, 7, 14 and 21 at 100 kHz. (b) The amount of ALP at different stages (control cells and cells at days 7 and 14). The error bars indicate the standard deviations.

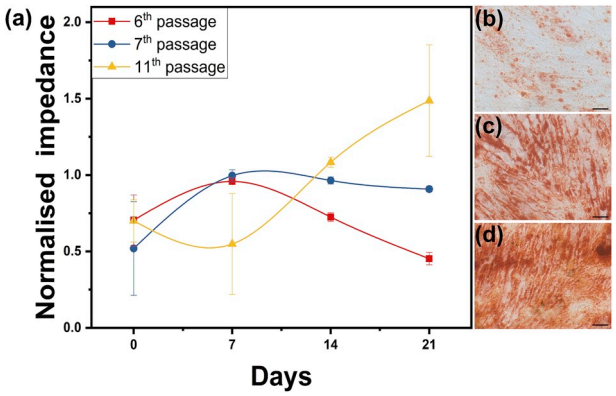

Fig. 7. (a) The impedance spectra of different cell generations at a frequency of 100 kHz. Images of calcium nodules dyed by Alizarin Red S of cells in the (b) eleventh passage, (c) seventh passage, and (d) sixth passage. The error bars indicate the standard deviations. The scale bars indicate 200 μm. (For interpretation of the references to color in this figure legend, the reader is referred to the Web version of this article.)

passages decreased gradually in a senescence-dependent manner. Overall, the change in impedance was consistent with the calcium nodule results.

3.6. Membrane capacity of single cells

While the cell membrane, which consists of a phospholipid bilayer, is responsible for the capacitive component of cell impedance, transmembrane ion channels and the cytoplasm contribute to the conductive component. Changes in the ion channel density on the cell membrane and fluctuations in the membrane potential through the regulation of biochemical exchanges between cells and their environment that contribute to cell permeability are often associated with carcinogenesis (Sundelacruz et al., 2009). An increase (Fig. 8) in the capacity of the cell membrane was observed as cells differentiated, which may correspond to the deterioration of the cell membrane permeability caused by calcification.

4. Conclusion

In summary, a biochip integrating droplet microfluidics and a microelectrode array was designed and fabricated to monitor the impedance of single cells undergoing osteogenic differentiation, and a cell droplet model based on a single-shell model was proposed. Single BM-MSCs were successfully captured in the proposed device, the impedance spectrum corresponding to each individual cell was monitored, and cell heterogeneity during differentiation was investigated. In principle, this system can be used to provide label-free and noninvasive electrical parameter measurements of individual cells and to investigate the heterogeneity of cells in a population due to single-cell trapping and impedance data acquisition. However, there are still some issues in this method that need to be solved in practical applications, such as throughput, those issues will be addressed in our further research. Besides, the proposed device can be adapted to monitor dynamic changes in the electrical properties of individual cells over long periods of time by integrating environmental (particularly temperature) controls within the device in the future.

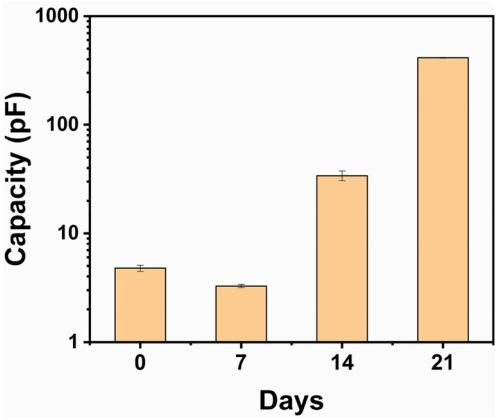

Fig. 8. The capacity of the cell membrane from days 0–21. As the cells differentiated, the capacitance increased. The error bars indicate the standard deviations.

Declaration of competing interest

The authors declare that they have no known competing financial interests or personal relationships that could have appeared to influence the work reported in this paper.

CRediT authorship contribution statement

Weihua Fan: Conceptualization, Methodology, Data curation, Writing - original draft. **Xi Chen:** Conceptualization, Methodology, Data curation, Writing - original draft. **Yuqing Ge:** Conceptualization, Data curation, Writing - review & editing, Supervision. **Yan Jin:** Supervision. **Qinghui Jin:** Project administration, Resources. **Jianlong Zhao:** Project administration, Resources.

Acknowledgments

W. Fan and X. Chen contributed equally to this work. This work was supported by the National Key Research and Development Program of China (No. 2018YFA0108202 and 2017 YFA 0205303), the National Natural Science Foundation of China (No. 61571429), and the Science and Technology Commission of Shanghai Municipality (No. 17JC1401001 and 18DZ1113002), STS Project of the Chinese Academy of Sciences (No. KFJ-STS-ZDTP-061), Research Project of Scientific Research Equipment of CAS (No. YJKYYQ20170043).

Appendix A. Supplementary data

Supplementary data related to this article can be found at https://doi.org/10.1016/j.bios.2019.111730.

References

Asami, K., 2002. J. Non-Cryst. Solids 305, 268–277.
Bian, X., Jing, F., Li, G., Fan, X., Jia, C., Zhou, H., Jin, Q., Zhao, J., 2015. Biosens. Bioelectron. 74, 770–777.
Casadevall i Solvas, X., deMello, A., 2011. Chem. Commun. 47, 1936–1942.
Chakraborty, I., Ricouvier, J., Yazhgur, P., Tabeling, P., Leshansky, A.M., 2019. Phys. Fluids 31, 022010.
Chen, J., Xue, C., Zhao, Y., Chen, D., Wu, M.H., Wang, J., 2015. Int. J. Mol. Sci. 16, 9804–9830.
Fan, W., Qiao, M., Jin, Y., Zhou, H., Ge, Y., Jin, Q., Zhao, J., 2019. J. Micromech. Microeng. 29, 035004.
Frank, O., Heim, M., Jakob, M., Barbero, A., Schafer, D., Bendik, I., Dick, W., Heberer, M., Martin, I., 2002. J. Cell. Biochem. 85, 737–746.
Gimsa, J., 2001. Bioelectrochemistry 54, 23–31.
Gosse, C., Croquette, V., 2002. Biophys. J. 82, 3314–3329.
Hankemeier, S., Keus, M., Zeichen, J., Jagodzinski, M., Barkhausen, T., Bosch, U., Krettek, C., Van Griensven, M., 2005. Tissue Eng. 11, 41–49.
He, M., Edgar, J.S., Jeffries, G.D.M., Lorenz, R.M., Shelby, J.P., Chiu, D.T., 2005. Anal. Chem. 77, 1539–1544.
Ishai, P.B., Sobol, Z., Nickels, J.D., Agapov, A.L., Sokolov, A.P., 2012. Rev. Sci. Instrum. 83, 083118.
Ishai, P.B., Talary, M.S., Caduff, A., Levy, E., Feldman, Y., 2013. Meas. Sci. Technol. 24.
Jansen, J.H., Jagt, O.P.v. d.J., Punt, B.J., Verhaar, J.A., Leeuwen, J.P.v., Weinans, H., Jahr, H., 2010. BMC Muscoskelet. Disord. 11, 188.
Kemna, E.W., Segerink, L.I., Wolbers, F., Vermes, I., van den Berg, A., 2013. Analyst 138, 4585–4592.
Kim, S.Y., Khanal, D., Kalionis, B., Chrzanowski, W., 2019. Nat. Protoc. 14, 576–593.
Kurz, C.M., Buth, H., Sossalla, A., Vermeersch, V., Toncheva, V., Dubruel, P., Schacht, E., Thielecke, H., 2011. Biosens. Bioelectron. 26, 3405–3412.
Kuznetsova, T.G., Starodubtseva, M.N., Yegorenkov, N.I., Chizhik, S.A., Zhdanov, R.I., 2007. Micron 38, 824–833.
Li, X., Soler, M., Szydzik, C., Khoshmanesh, K., Schmidt, J., Coukos, G., Mitchell, A., Altug, H., 2018. Small 14, e1800698.
Luo, T., Fan, L., Zhu, R., Sun, D., 2019. Micromachines 10, 104.
Luo, Y., Zhang, Y., Miao, G., Zhang, Y., Liu, Y., Huang, Y., 2019. Arch. Oral Biol. 97, 176–184.
Marcali, M., Elbuken, C., 2016. Lab Chip 16, 2494–2503.
Navas-Moreno, M., Chan, J.W., 2018. Methods Mol. Biol. 1745, 219–257.
Panke, O., Weigel, W., Schmidt, S., Steude, A., Robitzki, A.A., 2011. Biosens. Bioelectron. 26, 2376–2382.
Pauly, H., Schwan, H.P., 1959. Z. Naturforschung 14b, 125–131.
Petchakup, C., Li, K., Hou, H., 2017. Micromachines 8, 87.
Pinho, S., Frenette, P.S., 2019. Nat. Rev. Mol. Cell Biol. 20, 303–320.
Prodan, E., Prodan, C., John, H., Miller, J., 2008. Biophys. J. 95, 4174–4182.
Roy, S., Gao, Z., 2009. Nano Today 4, 318–334.
Saeys, Y., Van Gassen, S., Lambrecht, B.N., 2016. Nat. Rev. Immunol. 16, 449–462.
Safford, H.R., Bischel, H.N., 2019. Water Res. 151, 110–133.
Sano, M.B., Henslee, E.A., Schmelz, E., Davalos, R.V., 2011. Electrophoresis 32, 3164–3171.
Shapiro, H.M., 2003. Wiley-Liss.
Sundelacruz, S., Levin, M., Kaplan, D.L., 2009. Stem Cell Rev. 5, 231–246.
Tan, W.H., Takeuchi, S., 2007. Proc. Natl. Acad. Sci. 104, 1146–1151.
Tanyeri, M., Johnson-Chavarria, E.M., Schroeder, C.M., 2010. Appl. Phys. Lett. 96, 224101.
Tuma, P., 2017. J. Sep. Sci. 40, 940–947.
Vahey, M.D., Voldman, J., 2009. Anal. Chem. 81, 2446–2455.
Weyer, M., Jahnke, H.G., Krinke, D., Zitzmann, F.D., Hill, K., Schaefer, M., Robitzki, A.A., 2016. Anal. Bioanal. Chem. 408, 8529–8538.
Zhou, Y., Basu, S., Laue, E., Seshia, A.A., 2016. Biosens. Bioelectron. 81, 249–258.
Zrimsek, A.B., Chiang, N.H., Mattei, M., Zaleski, S., McAnally, M.O., Chapman, C.T., Henry, A.I., Schatz, G.C., Van Duyne, R.P., 2017. Chem. Rev. 117, 7583–7613.